

# All-Photon Bipolar Reversible Modulation Artificial Synapse for Color Perception and Mitigation of Glare Phenomenon

Haitao Dai (✉ [htdai@tju.edu.cn](mailto:htdai@tju.edu.cn))

Tianjin University

Yikai Fu

Tianjin University

Jia Li

Tianjin University

Changlei Wang

Soochow University <https://orcid.org/0000-0003-1257-627X>

Dewei Zhao

Sichuan University <https://orcid.org/0000-0001-7914-6288>

Xiaoli Zhang

Nanyang Technological University

Changlong Liu

Tianjin University

Qieni Lv

Tianjin University

Yong Wang

Tianjin University <https://orcid.org/0000-0003-4666-2053>

Yin Xiao

Tianjin University

Shouzhong Feng

Anhui Zhongyi New Materials Technology Co., Ltd



---

## Article

## Keywords:

**Posted Date:** November 7th, 2023

**DOI:** <https://doi.org/10.21203/rs.3.rs-3479435/v2>

**License:**   This work is licensed under a Creative Commons Attribution 4.0 International License.  
[Read Full License](#)

**Additional Declarations:** There is **NO** Competing Interest.

---

# **All-Photon Bipolar Reversible Modulation Artificial Synapse for Color Perception and Mitigation of Glare Phenomenon**

**Yikai Fu<sup>1</sup>, Haitao Dai<sup>1\*</sup>, Jia Li<sup>2</sup>, Changlei Wang<sup>3\*</sup>, Dewei Zhao<sup>4</sup>,  
Xiaoli Zhang<sup>5\*</sup>, Changlong Liu<sup>1</sup>, Qieni Lv<sup>2</sup>, Yong Wang<sup>6</sup>, Yin Xiao<sup>7</sup>  
and Shouzhong Feng<sup>8</sup>**

## **Author Information**

---

### **Affiliations**

**<sup>1</sup>Tianjin Key Laboratory of Low Dimensional Materials Physics and Preparing  
Technology, School of Science, Tianjin University, Tianjin 300072, China**

Y. Fu, H. Dai, C. Liu

**<sup>2</sup>Key Laboratory of Optoelectronics Information Technology, Ministry of Education,  
School of Precision Instrument and Optoelectronics Engineering, Tianjin University,  
Tianjin 300072, China**

J. Li, Q. Lv

**<sup>3</sup>School of Optoelectronic Science and Engineering, Collaborative Innovation Center of  
Suzhou Nano Science and Technology, Key Lab of Advanced Optical Manufacturing  
Technologies of Jiangsu Province, Key Lab of Modern Optical Technologies of Education  
Ministry of China, Soochow University, Suzhou 215006, China**

C. Wang

**<sup>4</sup>College of Materials Science and Engineering, Engineering Research Center of  
Alternative Energy Materials & Devices, Ministry of Education, Sichuan University,  
Chengdu 610065, China**

D. Zhao

**<sup>5</sup>School of Physics and Opto-electronic Engineering, Guangdong Province Key  
Laboratory of Information Photonics Technology, Guangzhou 510006, China**

X. Zhang

<sup>6</sup>Department of Chemistry, School of Science, Tianjin University, Tianjin 300075, China

Y. Wang

<sup>7</sup>School of Chemical Engineering and Technology, Tianjin University, Tianjin 300350,  
China

Y. Xiao

<sup>8</sup>Anhui Zhongyi New Materials Technology Co., Ltd, Chuzhou 239599, Anhui, China

S. Feng

## Contributions

Y. Fu prepared the devices, integrated the contents of optical and electrical measurements, and conducted the entire paper writing. H. Dai organized the ideas and logic of overall paper. J. Li and Q. Lv provided the optical testing work. C. Wang, D. Zhao, and X. Zhang contributed to the material synthesis work. Y. Wang and Y. Xiao offered guidance on the thermal evaporation electrode method. S. Feng contributed to the work related to the visual nerve. All authors have discussed the results and commented on the manuscript.

## Corresponding author

Correspondence to: H. Dai ([htdai@tju.edu.cn](mailto:htdai@tju.edu.cn)), C. Wang ([cl.wang@suda.edu.cn](mailto:cl.wang@suda.edu.cn)) & X. Zhang ([xlzhang@tju.edu.cn](mailto:xlzhang@tju.edu.cn))

## Abstract

---

The focus of artificial synaptic device researches has gradually shifted towards synaptic devices with specific functionalities. In this work, we report an optically responsive memristor (with a

configuration of Ag:AgI/MA<sub>0.4</sub>FA<sub>0.6</sub>PbI<sub>3</sub>/Ag:AgI) that achieves bidirectional switching of resistive states utilizing 450 nm and 650 nm light at an ultra-low readout voltage of 0.001 V. The device presents artificial visual synapses (AVS) features in terms of short-term plasticity (STP)/long-term plasticity (LTP) to pulsed light in the range of 300-700 nm. Under 450 nm blue light, an abrupt shift from low to high resistance can be observed, resembling the effect of glare. Intriguingly, the introduction of 650 nm red light can expedite the recovery following blue light exposure. These attributes underscore potential of the device for tasks encompassing color recognition, memory functions, and adaptation, suggesting promising prospects within artificial visual neural networks for ultraviolet and visible light sensing, transmission, and memory applications.

## Introduction

---

The rapid development of artificial intelligence (AI) and machine learning has introduced formidable challenges to conventional computing paradigms, stemming from the escalating volumes of data to be processed. Traditional architectures, limited by the von Neumann bottleneck<sup>1</sup>, where computation and memory are segregated, result in significant energy consumption and time overheads during advanced tasks such as machine learning and image recognition. In contrast, the "memory processing" mechanism of the human brain accelerates processing speed while significantly reducing energy consumption<sup>2</sup>. To emulate this neural computing paradigm, researchers have increasingly turned their focus toward memristors. These novel devices are also referred to as artificial synapses due to their synaptic characteristics resembling neural structures<sup>3-5</sup>.

Artificial synapses have developed into many types, among which artificial visual synapses (AVS) that encompass optical sensing and memory capabilities have received widespread attention. The approach of biomimicking the biological visual neural system using these synapses has been extensively applied<sup>6,7</sup>. AVS can be categorized based on their structure into two distinct types: standalone devices featuring separate light-sensing and memory modules<sup>8,9</sup>, and integrated devices combining both light sensing and memory modules into one unit<sup>10-13</sup>. It is evident that the latter option offer advantages for achieving low-power

consumption and large-scale integration.

In order to enhance the capabilities of AVS, improving the performance and expanding the functionality of optoelectronic materials are the key pathways. Many low-dimensional optoelectronic materials have already been employed in optimizing artificial visual neural systems<sup>14-16</sup>. Perovskites materials have also been considered as the promising candidate for AVS applications due to the outstanding optoelectronic properties and characteristics related to ion migration<sup>17-28</sup>.

Many types of AVS, e.g. low-dimensional, perovskite materials etc., have been reported and exhibit varieties of functions, such as image recognition and memory. The narrow range of their light response, however, poses a challenge in replicating functions akin to those of the human eyes<sup>14-28</sup>. Additionally, most of the reported AVS presented single function related to illuminating light. While natural synapses are categorized into two types, i.e. excitatory and inhibitory synapses<sup>29,30</sup>. Excitatory synapses make up the majority of synaptic connections in the nervous system, a small fraction of inhibitory synapses play an indispensable role. Inhibitory synapses shape the brain's circuitry connections and dynamic changes through synaptic plasticity. The imbalance between excitatory and inhibitory synapses is a crucial mechanism underlying neuropsychiatric disorders such as autism and depression<sup>31</sup>. Inhibitory synapses are essential for establishing excitatory/inhibitory (E/I) balance, achieving firing rate homeostasis, controlling excitatory plasticity, and shaping neural network connections<sup>32</sup>. Hence, achieving bipolar synaptic plasticity is a focal point in AVS. Currently, the bipolar reversible modulation of AVS is primarily achieved through a combination of optical and electrical stimulation<sup>33,34</sup>. This hybrid signaling method results in notable energy consumption, introduces system complexity, and imposes restrictions on modulation speed. The achievement of all-optical bidirectional reversible synaptic plasticity stands as a universally acknowledged challenge for AVS<sup>35,36</sup>.

In this work, we engineer an all-optical bipolar reversible modulation memristor, which works on the photoinduced reversible switching effect between Ag and abundant iodine ion on the prepared perovskites film. Our device demonstrates the capability of AVS to recognize and retain information about electromagnetic waves across the ultraviolet to visible light spectrum. Notably, it rapidly transitions from a low to high resistance state when exposed to 450 nm blue

light, gradually reverting to the low resistance state in the absence of light, and efficiently recovering it through 650 nm red light irradiation. Functioning at an ultra-low readout voltage of 0.001 V, the device achieves exceptional all-optical bidirectional reversible regulation of resistive states, boosting an impressive high-to-low resistance switching ratio up to 74459 at the readout voltage of 0.01 V. These findings underscore the successful realization of a fully photonically controlled artificial synapse with dual-polarity reversibility and ultra-low energy consumption, showcasing its potential for UV-to-visible light sensing, memory storage, and adaptive functionalities.

## Results

**Characteristics of Ag:AgI/MA<sub>0.4</sub>FA<sub>0.6</sub>PbI<sub>3</sub>/Ag:AgI optically responsive memristor.** As shown in Fig. 1a, a typical device configuration consisted of an approximately 600 nm thick MA<sub>0.4</sub>FA<sub>0.6</sub>PbI<sub>3</sub> film spun onto a glass substrate, and two Ag electrodes of size 2.75 × 2 mm<sup>2</sup> and thickness 200 nm, spaced 100 μm apart. Fig. 1b presents the cross-sectional SEM image of the device, showing the perovskite film thickness of approximately 600 nm and Ag thickness of 200 nm. The MA<sub>0.4</sub>FA<sub>0.6</sub>PbI<sub>3</sub> film utilized in this study was prepared using one-step spin-coating method<sup>37</sup>. Detailed can be found in the methods section. Fig. 1c displays a top-view scanning electron microscopy (SEM) image of MA<sub>0.4</sub>FA<sub>0.6</sub>PbI<sub>3</sub> film. It is evident that uniform micrometer-sized grains are passivated at the grain boundaries by excess PbI<sub>2</sub><sup>37</sup>. In Supplementary Figure1, the EDS image of the thin film reveals the reduction of Pb and I elements and the deficiency of N elements at grain boundaries. It further confirms the formation of PbI<sub>2</sub> at grain boundaries. The X-ray diffraction pattern in Fig. 1d confirms the crystallinity of the perovskite film, with peaks around 14° and 28° corresponding to (110) and (220) diffraction peaks<sup>38</sup>. The green and blue lines represent standard PDF cards (PDF#97-025-2413 and PDF#97-025-0740) for MAPbI<sub>3</sub> and FAPbI<sub>3</sub>, respectively. The good agreement of diffraction peaks of our film with these standards indicates the successful fabrication of the MA<sub>0.4</sub>FA<sub>0.6</sub>PbI<sub>3</sub> film. Other major peaks, except those shown by the red line corresponding to the diffraction peaks of PbI<sub>2</sub> (PDF#97-006-8820), also match well. This suggests substantial presence of residual PbI<sub>2</sub> on the film surface, which can be ascribed to the usage of Pb(SCN)<sub>2</sub>

as the additive<sup>39</sup>.

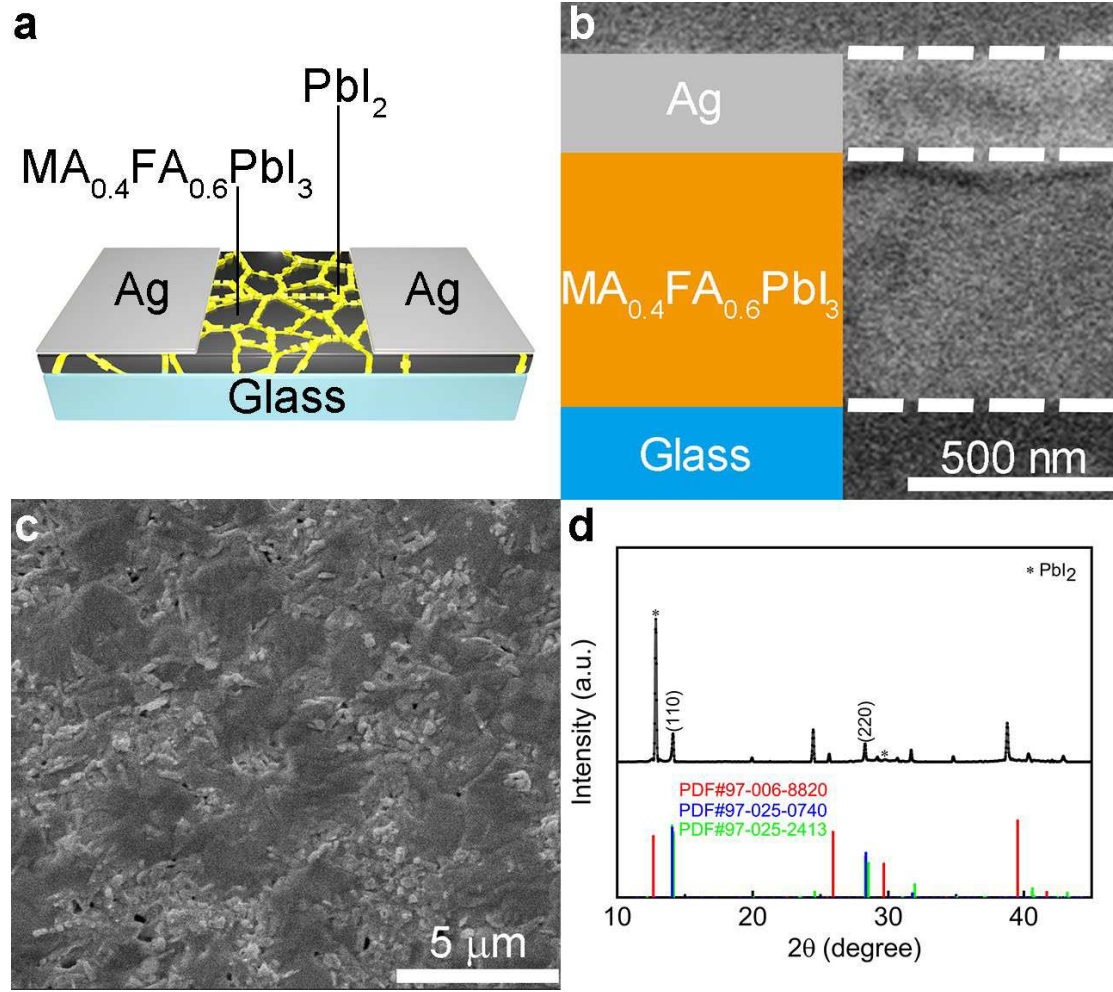


**Fig. 1** Structure and composition of  $\text{Ag:AgI/MA}_{0.4}\text{FA}_{0.6}\text{PbI}_3/\text{Ag:AgI}$  optically responsive memristor. **a** Schematic structure of the device. **b** Cross-sectional view SEM image of the device. **c** Top-view SEM image of the  $\text{MA}_{0.4}\text{FA}_{0.6}\text{PbI}_3$  film. **d** XRD spectrum of the  $\text{MA}_{0.4}\text{FA}_{0.6}\text{PbI}_3$  film.

Fig. 2a illustrates a remarkable feature of the device, showcasing nearly three orders of magnitude in both inhibition and enhancement across the bipolar spectral response, spanning from ultraviolet to visible light wavelengths (300-800 nm). To explore the underlying causes behind this peculiar photocurrent spectrum, we fabricated devices with Au electrodes for comparative analysis. The results indicate that devices with Au electrodes exhibit gain-only optical response characteristics within the same spectral range (see Supplementary Figure2). Additionally, through I-V curves we discovered that devices with Ag electrodes exhibited exceptionally increased dark current compared to those with Au electrodes (see Supplementary Figure3). These attributes primarily arise from the formation of abundant AgI due to the



reaction (see equation (1)) between Ag and PbI<sub>2</sub> on the surface of the perovskite film during the process of depositing Ag electrodes. It is significantly different from the phenomenon observed in traditional perovskite devices with Ag as the electrode. In the latter devices, following perovskite film degradation and the subsequent formation of AgI through electrode reaction, there is a distinct rise in device resistance accompanied by a decline in overall performance<sup>40-43</sup>. Two key points support this assertion: 1. AgI serves as a highly conductive ionic conductor notably amplifies the conductivity of the device<sup>44,45</sup>; 2. The I-V hysteresis curves of the device under both  $\pm 2$  V and  $\pm 10$  V conditions prominently demonstrate distinctive Nonlinear Differential Resistance (NDR) effect (see Supplementary Figure4a and 4b). This phenomenon is exclusive to AgI-based devices<sup>46-49</sup>.

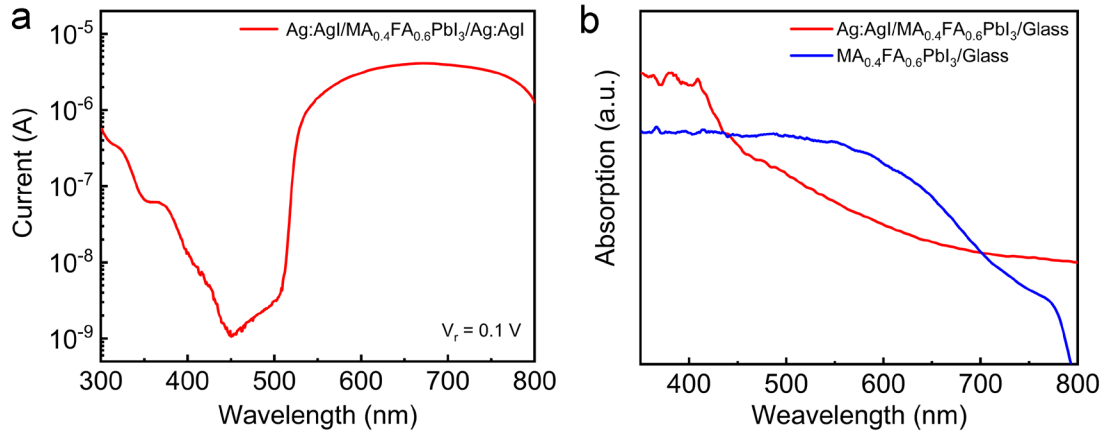


**Fig. 2** The photocurrent spectrum and light absorption spectrum of the Ag:AgI/MA<sub>0.4</sub>FA<sub>0.6</sub>PbI<sub>3</sub>/Ag:AgI optically responsive memristor. **a** Photocurrent spectrum of the device,  $V_r = 0.1$  V. **b** Absorption spectra of the MA<sub>0.4</sub>FA<sub>0.6</sub>PbI<sub>3</sub> film and electrode region of the device.

Afterwards, we delved deeper into the underlying causes of the unique spectral response features displayed by the device. According to Fig. 2a, the current of the device experiences a significant decline when exposed to 300-500 nm light. This phenomenon demonstrates a noteworthy erasure effect, which can be attributed to the decomposition of AgI and the formation of I<sub>2</sub> (see equation (2)) at the interface between the electrode and the film for the light absorption (see Fig. 2b) and photosensitive nature of AgI<sup>50</sup>. Under continuous light in the range of 300-500 nm exposure, the device maintains an elevated high-resistance state. The cessation

of light exposure prompts the newly generated  $I_2$  to react with Ag, regenerating AgI<sup>51</sup> (see equation (3)). This gradual process facilitates the return of the device to its low-resistance state prior to light exposure.



Intriguingly, when the device in the high-resistance state is irradiated with light in the 500-700 nm range, it swiftly reverts to the low-resistance state before light exposure (see Fig. 2a). Furthermore, with the variation of the morphology and distribution of  $PbI_2$  on the surface of the perovskite thin film, the photocurrent spectrum of devices exhibits distinct characteristics (see Supplementary Figure5). Several factors contribute to this phenomenon: 1. Decreased photosensitivity of AgI in this wavelength range<sup>50</sup>, leading to the reformation of AgI as some  $I_2$  reacts with Ag; 2. Strong absorption and photocurrent response of the perovskite film in this range (see Fig. 2b), offsetting the conductivity decline resulting from AgI decomposition; 3. Light irradiation within this spectral range reduces the activation energy for iodine ion migration in the polycrystalline perovskite film<sup>52</sup>, facilitating the migration of iodine ions in the perovskite film. These ions react with Ag, resulting in the reformation of AgI. The operating mechanism of the device is shown in Fig. 3.

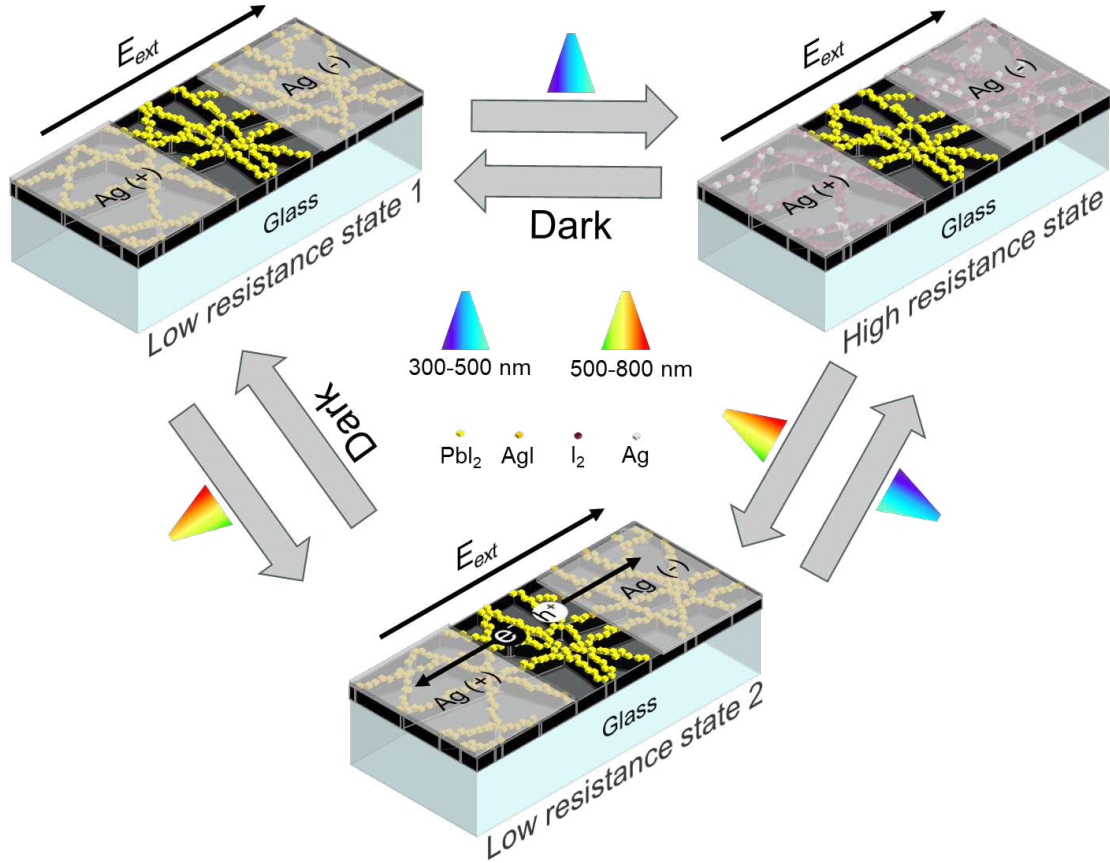


**Fig. 3** Schematic representation of device operation mechanism.

To verify the photosensitive memristor characteristics of the device, we conducted three cycles of I-V measurements under dark and different light illumination conditions separately (see Fig. 4). Under dark conditions, the device exhibited linear Ohmic contact characteristics within the scanning voltage range from -0.01 to 0.01 V, without any observed hysteresis (see Fig. 4a). This indicates that the scanning voltage range from -0.01 to 0.01 V is insufficient to induce the NDR effect of AgI.

But during the forward-reverse sweep process within the voltage range of 0.01 to -0.01 V, when the device was illuminated with 650 nm light at the illumination of  $16.7 \text{ mWcm}^{-2}$ , its resistance decreased slightly, exhibiting a smaller hysteresis loop in the I-V curve (see Fig. 4b). However, when the device was exposed to 450 nm light at the illumination of  $1.86 \text{ mWcm}^{-2}$  during the -0.01 to 0.01 V forward sweep, it rapidly switched to a high-resistance state (see Fig. 4c). Upon stopping the light illumination at the beginning of the 0.01 to -0.01 V reverse sweep, the device gradually recovered to a low-resistance state, showing a slightly larger hysteresis loop in the I-V curve (see Fig. 4c). Finally, when 450 nm and 650 nm light were separately

applied during the forward and reverse sweep processes, the I-V curve exhibited the characteristic behavior of a memristor<sup>53</sup> (see Fig. 4d).

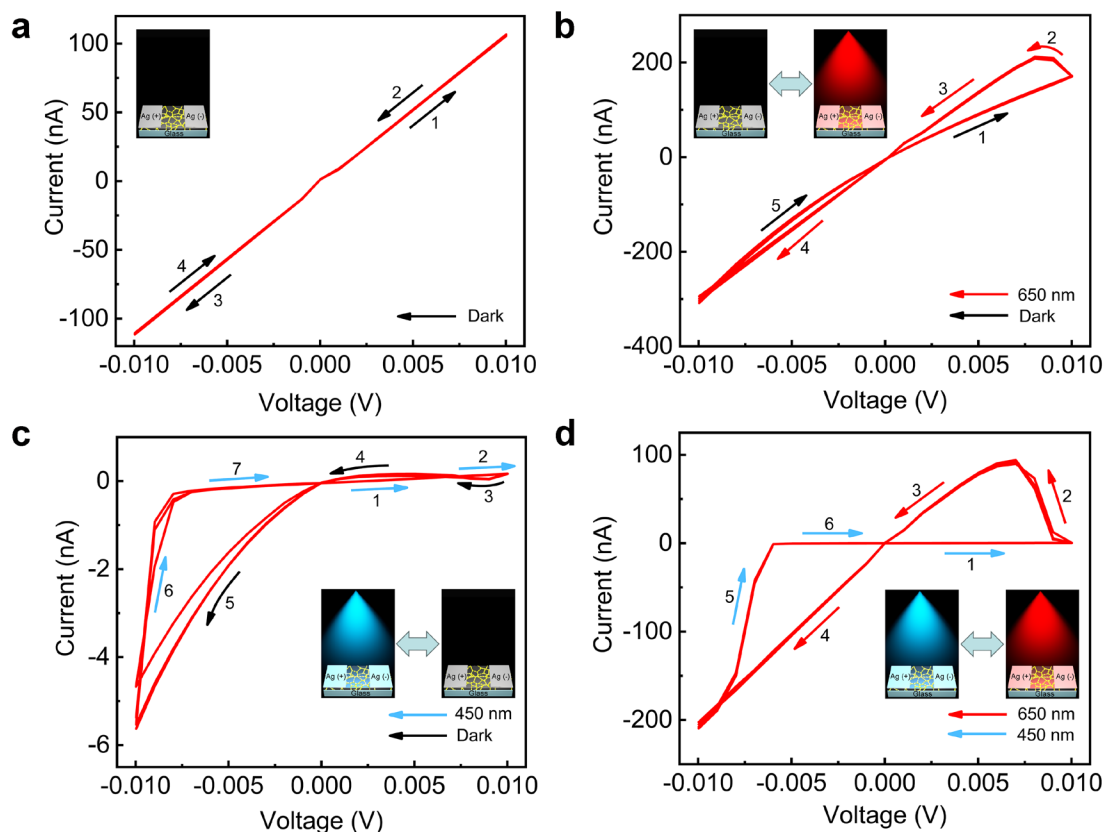


**Fig. 4** Illumination-affected I-V hysteresis curves. (Illustrations show the device testing schematic under different conditions of darkness, 650 nm at the illumination of  $16.7 \text{ mWcm}^{-2}$ , and 450 nm at the illumination of  $1.86 \text{ mWcm}^{-2}$ ). **a** I-V characteristics under dark conditions. **b** I-V characteristics under dark and 650 nm light illumination. **c** I-V characteristics under dark and 450 nm light illumination. **d** I-V characteristics under 450 nm and 650 nm light illumination. (Arrows indicate the voltage scanning sequence and testing conditions.)

Next, stability testing of the device was performed. A total of 180 I-V cycles were conducted using the same testing methodology as shown in Fig. 4d. While during the initial 40 cycles, the device exhibited a gradual decrease in low-resistance current and an increase in high-resistance current, resulting in a gradual reduction of the high-low resistance switching ratio to around  $10^2$  (see Fig. 5a). Amazingly, after 40 cycles, the device gradually stabilized, and even up to the 180th cycle, there was minimal variation in the high-low resistance switching ratio (see Supplementary Figure7a). This observation indicates that within the -0.01 V to 0.01 V scanning voltage range, the device is capable of repetitively and stably switching between

high and low resistance states, triggered by illumination with 450 nm and 650 nm light (switching speed: 40 nm/s). Subsequently, endurance test was conducted on the device. At the readout voltage of 0.001 V, the device exhibited extremely stable switching behavior of its high and low resistance states within 4800 s interval, as the 450 nm and 650 nm light alternated (see Fig. 5b).

We observed that the magnitude of hysteresis in the I-V curve of the device could be adjusted by varying the scan time. We tested the device with different scan speeds (see Supplementary Figure8a). The results indicated that longer scan time, resulted in "fat" curves and higher high-to-low resistance ratios. This phenomenon is attributed to prolonged blue light exposure leading to increased AgI decomposition, resulting in more  $I_2$  generation and higher device resistance. Conversely, longer red-light exposure favors AgI re-synthesis, causing the device to recover to lower resistance state.

Subsequently, we expanded the scanning voltage range from -0.2 V to 0.2 V for further I-V cyclic scanning tests (see Supplementary Figure9). This device showed Ohmic contact characteristics (see Supplementary Figure9a) under dark condition. But when 450 nm and 650 nm light were separately illuminated during the forward and reverse sweep processes, our device exhibited larger high-low resistance switching ratio (see Fig. 5c). At the readout voltage of 0.01 V, the high-low resistance ratio of the device consistently remained close to  $10^4$  over 50 cycles of I-V testing (see Supplementary Figure7c), with the highest switching ratio reaching 74459. As the number of I-V cycles increased, the device demonstrated an increasingly stable high-low resistance switching ratio (see Fig. 5c). The final 10 I-V cycle scan curves complete overlap (see Fig. 5d), indicating enhanced stability at 0.01 V readout voltage. Following this, endurance testing of the device was conducted at the readout voltage of 0.1 V (see Supplementary Figure7b).

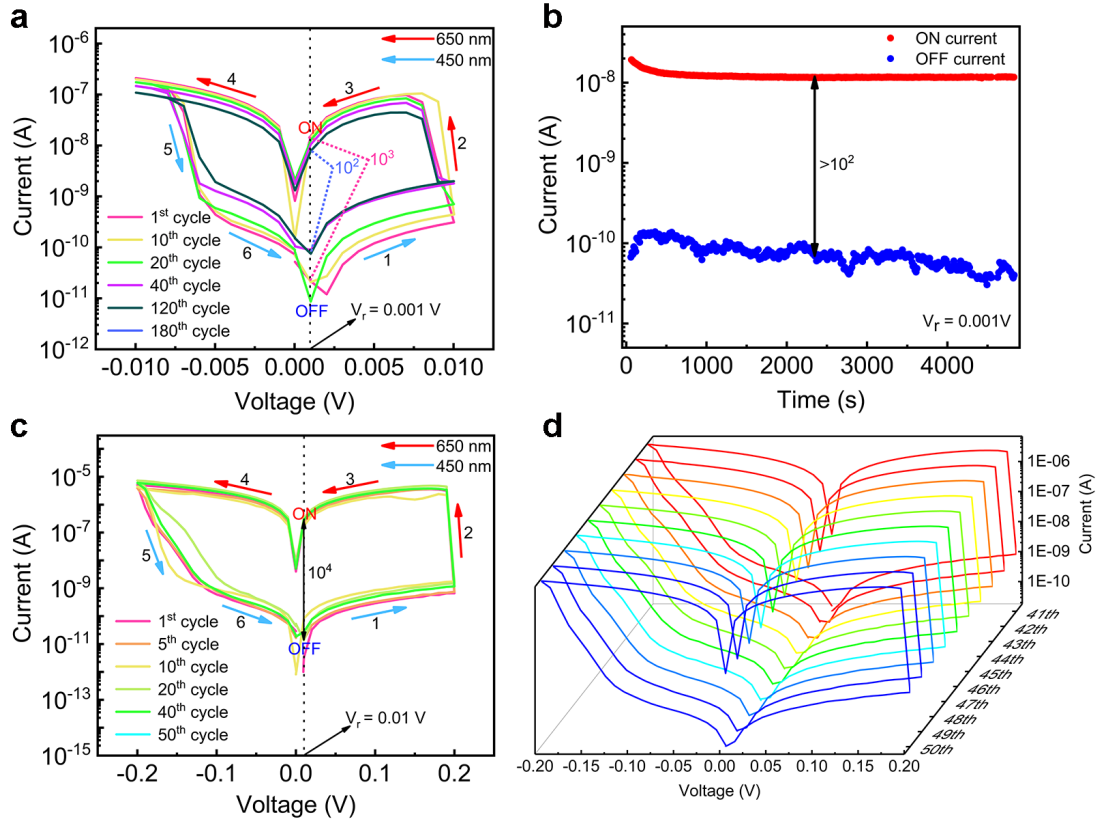


**Fig. 5** Light-modulated I-V cyclic curves and endurance testing. **a** I-V cyclic curves were recorded for the 1st, 10th, 20th, 40th, 120th, and 180th cycles under a scanning voltage range from -0.01 to 0.01 V (average scanning speed: 100 s/cycle). **b** Endurance assessment involved alternating illumination of 450 nm and 650 nm light at the readout voltage of 0.001 V (wavelength switching speed: 40 nm/s). **c** I-V cyclic curves were recorded for the 1st, 5th, 10th, 20th, 40th, and 50th cycles under a scanning voltage range from -0.2 to 0.2 V (average scanning speed: 420 s/cycle). **d** I-V cyclic curves were measured for cycles 41 to 50 under a scanning voltage range from -0.2 to 0.2 V.

**Color Perception and memory.** Based on the previous measurements, we observed that our device exhibits all-optical bidirectional reversible regulation of resistive states when stimulated with light in the range of 300-800 nm. Furthermore, it demonstrates stable high resistance and low resistance states under continuous stimulation with light at 450 nm and 650 nm, respectively. This light-induced response exhibited by the device bears resemblance to the adaptability process observed in the human eyes when exposed to light. In the realm of human perception, vision plays a pivotal role, accounting for a substantial 80% or more of the

information gleaned from external stimuli. Visual sensing and memory significantly influence human life, work, and learning. Light traverses the cornea and pupil, subsequently refracted by the lens to project onto the retina. Photoreceptor cells—cones and rods—residing within the retina relay stimuli through neural synapses to the optic nerve, which ultimately transmits postsynaptic current (PSC) to the cerebral visual center, culminating in the human visual experience. Within this intricate process, cones and rods serve as critical photoreceptors, with cones, particularly, responsible for color vision<sup>54</sup>. In the pursuit of photonic artificial synapses to facilitate visual sensing and memory, biomimetic emulation of cone cells is of paramount significance. As depicted in Fig. 6a, the transmission of light-stimulated signals by cone cells entails the release of neurotransmitters from the presynaptic membrane of cones upon light signal excitation, subsequently binding to active receptors on the postsynaptic membrane of bipolar cells, thereby eliciting variations in PSC<sup>54</sup>.

Our device exhibits functionalities akin to visual synaptic between cones and bipolar cells. As illustrated in Fig. 6b and c, when subjected to pulse light stimuli with pulse widths of 10 ms and 50 ms in the range of 300-700 nm, the device demonstrates wavelength-resolved short-term plasticity (STP). Subsequently, employing a sequence of 50 pulses with pulse widths of 100 ms and intervals of 100 ms, under light in the 300-700 nm range, the device manifests wavelength-dependent long-term plasticity (LTP), as depicted in Fig. 6d. This plasticity may stem from the migration of Ag ions and I ions<sup>55</sup>, in conjunction with variations in the generation and decomposition rates of AgI under different wavelength light exposures. Through this testing regimen, it was ascertained that the device exhibits a discerning capability for distinct visible light pulse wavelengths, even as brief as 10 ms (see Fig. 6b). Furthermore, as the pulse width (see Fig. 6c) and frequency (see Fig. 6d) increase, the color resolution capacity of the device becomes augmented.

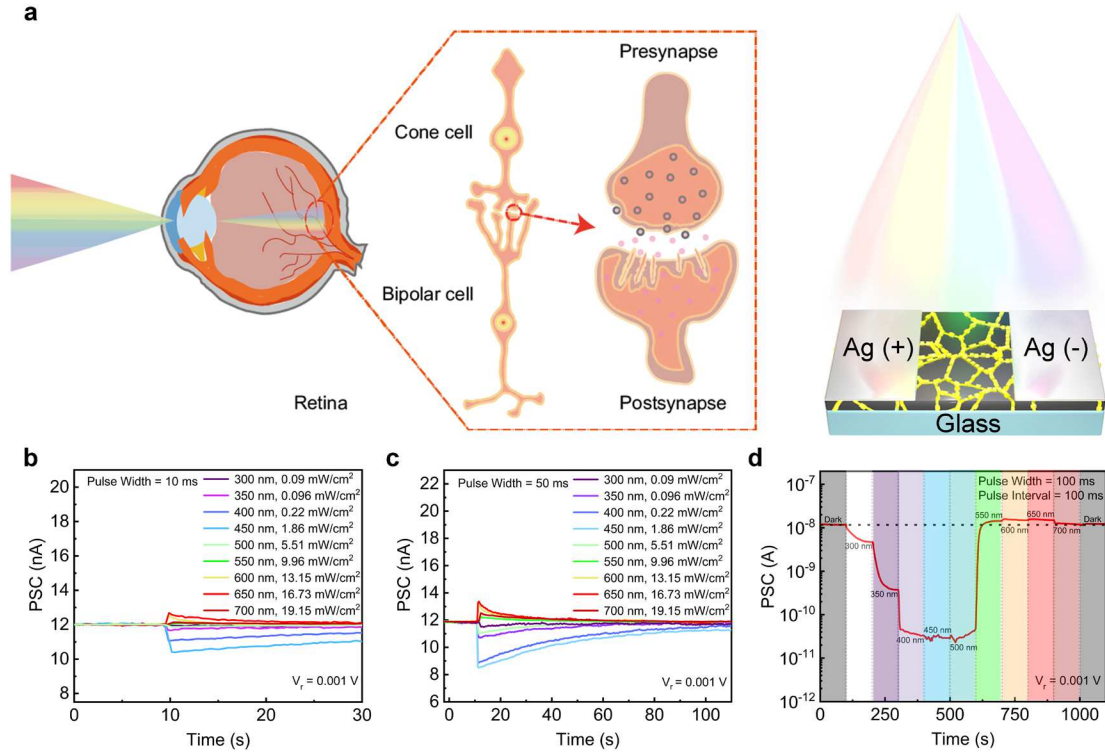


**Fig. 6** Schematics and characteristics of color perception and memory based on AVS. **a** Color recognition process of the biological visual neural synapse (left) and schematic representation of color recognition testing using all-photon artificial synaptic devices (right). PSC following **b** 10 ms and **c** 50 ms pulse light stimulations at wavelengths of 300 nm, 350 nm, 400 nm, 450 nm, 500 nm, 550 nm, 600 nm, 650 nm, and 700 nm. **d** PSC following a series of 50 pulse light trains, sequentially irradiated at 300 nm, 350 nm, 400 nm, 450 nm, 500 nm, 550 nm, 600 nm, 650 nm, and 700 nm, with a pulse width and interval of 100 ms each.

Remarkably, the device demonstrates excitatory postsynaptic currents in response to warm-colored light (550-700 nm) stimulation, while exhibiting inhibitory postsynaptic currents upon near-ultraviolet and cool-colored light (300-500 nm) stimulation. Thus, the emulation of both excitatory and inhibitory synaptic processes in humans is realized solely through photonic stimuli, thereby achieving a bionic implementation of bipolar artificial synapses under full optical control. Additionally, blue light exposure can lead to irreversible retinal damage<sup>56</sup>, and research conducted by the University of London in 2021 indicates that timed exposure to red light can enhance vision<sup>57</sup>. Our device exhibits features akin to human eyes under these two illumination conditions.

**Adaptive processes and mitigation of glare phenomenon.** As depicted in Fig. 7a, through



toggling between three conditions—650 nm, 450 nm, and darkness—the device emulates the reversible transitions observed in human vision during the adaptive process under red and blue light stimuli, yielding four distinct states. With respective thresholds of 12.5 nA and 11 nA for "clear" and "blurry" vision (indicated by red and blue dashed lines in Fig. 7b-e), the device attains "clear" and "blurry" states under red and blue light stimulation of 10, 50, and 100 ms, respectively. Moreover, as the stimulus duration increases, two states of the device intensify, extending the adaptation time (see Fig. 7b). Notably, following a 100 ms pulse light stimulus, the device takes approximately 500 s to recover to the baseline state.

Continuing our investigation, we proceeded to delve into the adaptive processes of artificial synapses under the influence of consecutive pulsed light stimulation, illustrated in Supplementary Figure 11a and b. This phenomenon, referred to as paired-pulse facilitation (PPF), stems from the transient enhancement in vesicular release probability at synapses during continuous stimulation<sup>58</sup>. In our artificial synapses, this phenomenon can be conceptualized as the immediate modulation of AgI content in response to consecutive stimulation. Upon applying pairs of sequential red light and blue light pulses to the artificial synapses, the PSC elicited by the second pulse exhibited distinct enhancements and reductions relative to those prompted by the first pulse. To quantitatively evaluate the PPF induced by PSCs, we established a PPF index that quantifies the ratio between the amplitudes of the second postsynaptic current (A2) and the first postsynaptic current (A1). Under the influence of 650 nm red light and 450 nm blue light stimulation, the PPF index progressively diminished as the time interval between the two stimuli ( $\Delta t$ ) increased, as depicted in Supplementary Figure 11c and d. Further extension of the stimulus duration reveals a transient "blind" under 30 pulses of blue light with a pulse width of 100 ms and intervals of 100 ms, leading to a reduction in response current to zero (see Fig. 7c). This phenomenon mirrors the transient "glare effect"<sup>59</sup> experienced by drivers transitioning from bright environments to tunnels, emulating the adaptive process of the human eye. The distinctive aspect of this device lies in its capability to rapidly restore vision from a "blind" state to a "clear" state using 650 nm red light stimulation following prolonged exposure to 450 nm blue light (see Fig. 7d, e). This characteristic holds tremendous potential for future specialized functionalities in AVS and mitigation of the "glare effect" in human eyes.

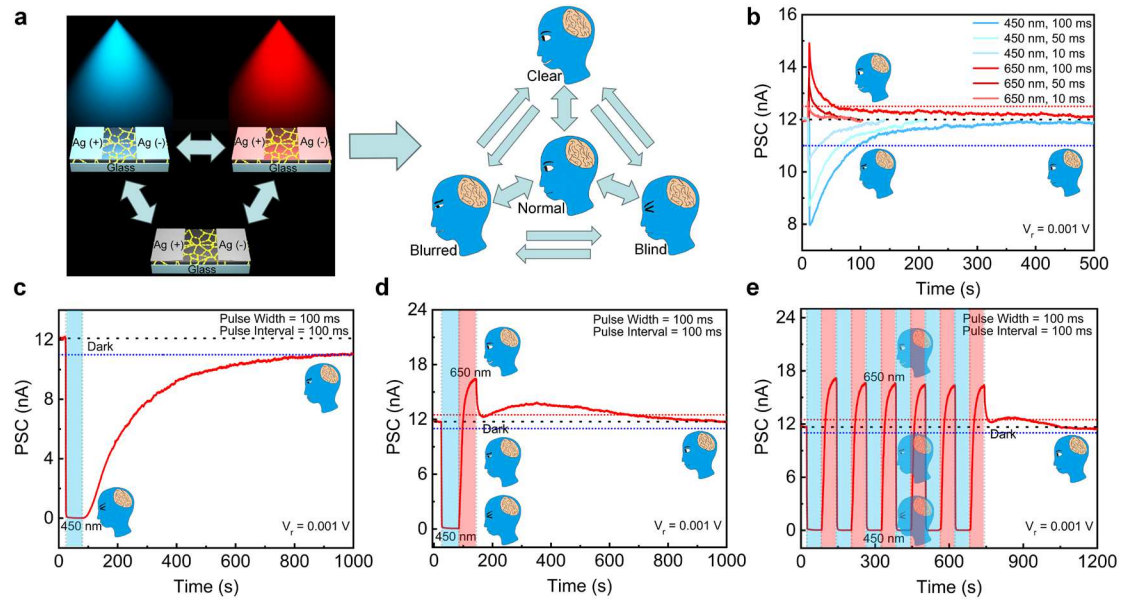


**Fig. 7** The adaptive processes of AVS after 450 nm and 650 nm light stimulations. **a** Schematic illustration of the all-optical artificial synapse mimicking the adaptive process in humans after 450 nm and 650 nm light stimulations. **b** PSC of the artificial synapse devices after 450 nm and 650 nm pulsed light stimulations, with pulse durations of 10 ms, 50 ms, and 100 ms, respectively. **c** PSC of the artificial synapse devices under 450 nm pulsed light stimulation with a sequence of 30 pulses, each having a pulse width and interval of 100 ms. **d** PSC of the artificial synapse under the sequential illumination of 30 pulses of 450 nm and 650 nm light with a pulse width and interval both set at 100 ms. **e** Six cycles of **d**.

## Discussion

We demonstrated a memristor that achieved all-optically bidirectional reversible regulation of resistive states. By leveraging the differences in photoresponsive ranges between AgI and  $\text{MA}_{0.4}\text{FA}_{0.6}\text{PbI}_3$  films, our device exhibits bipolar response characteristics of inhibition and gain under two distinct frequency ranges: 300-500 nm and 500-800 nm, respectively. By applying 450 nm and 650 nm light exposures, stable switching of resistive states is achieved at an ultra-low readout voltage of 0.001 V, yielding a remarkable high-low resistance switching ratio of up to 74459 at the readout voltage of 0.01 V. Additionally, through further investigation, our device demonstrates discernible synaptic memory-like attributes in response to pulsed light within the 300-700 nm wavelength range, showcasing significant potential for specialized AVS with color

recognition capability. Moreover, our work emulates the adaptive process of human eyes to red and blue light stimulation. Similar to human eyes, our artificial synaptic device manifests features of improved vision under red light and reduced vision under blue light. Intriguingly, after prolonged exposure to blue light-induced "blind", our device remarkably regains functionality upon swift stimulation with red light. The distinctive characteristics of our device offer substantial potential applications in color recognition, memory, and mitigating the effects of glare in human vision.

## Methods

---

**Fabrication and characterization of AVS.**  $\text{PbI}_2$  and MAI were dissolved in a mixed solvent of DMF and DMSO at a molar ratio of 1:1. Additionally, 3 wt%  $\text{Pb}(\text{SCN})_2$  was added as an additive to the solution to obtain the  $\text{MAPbI}_3$  solution. Using the same procedure, FAI was dissolved to prepare the  $\text{FAPbI}_3$  solution. Subsequently, the  $\text{MAPbI}_3$  and  $\text{FAPbI}_3$  solutions were mixed in 4:6 ratio to obtain the  $\text{MA}_{0.4}\text{FA}_{0.6}\text{PbI}_3$  precursor solution with a concentration of 3M. Sodium calcium glass substrates were sequentially cleaned with detergent, water, alcohol, and acetone, then subjected to ultrasonic bath deposition. Subsequently, they were treated with UV-ozone cleaner to remove organic residues and enhance surface wettability. The precursor solution (50  $\mu\text{l}$ ) was spin-coated onto the glass substrate using an antisolvent method. This involved an initial spin at 500 rpm for 3 s followed by 4000 rpm for 60 s, with the controlled addition of 600  $\mu\text{l}$  of diethyl ether as an anti-solvent at specific intervals during the spin process<sup>60</sup>. The deposited intermediate perovskite films were annealed on a hotplate at 80 °C for 2 minutes and then further annealed at 150 °C for 5 minutes. All procedures were carried out in a nitrogen-filled glovebox. Finally, a 200 nm-thick silver layer was evaporated onto the top of the perovskite layer using a mask. The electrical characterization of the devices was conducted by employing Keithley 4200s A semiconductor parameter analyzer system, which was connected to a microprobe station positioned within a dark enclosure. The perovskite film and device absorption spectra were characterized using a UV-visible spectrophotometer (UV-3600 PC). Spectral response, I-V curves under illumination, and pulse light response tests were carried out using programmed monochromator, optical shutter, and semiconductor parameter

analyzer (broadband visible light generated by a halogen lamp). Scanning electron microscopy (SEM) images of the films and devices were obtained using a Thermo Scientific™ Apreo SEM at 15 kV. X-ray photoelectron spectroscopy (XPS) characterization was performed using Thermo K-Alpha+ system.

## Data Availability Statement

The data that support the findings of this study are available from the corresponding author upon reasonable request.

## References

1. Ohno, T. et al. Short-term plasticity and long-term potentiation mimicked in single inorganic synapses. *Nat. Mater.* **10**, 591-595 (2011).
2. Nowakowski, T. J. Building blocks of the human brain. *Science* **362**, 169-169 (2018).
3. Jo, S. H. et al. Nanoscale memristor device as synapse in neuromorphic systems. *Nano Lett.* **10**, 1297-1301 (2010).
4. Pickett, M. D., Medeiros-Ribeiro, G. & Williams, R. S. A scalable neuristor built with Mott memristors. *Nat. Mater.* **12**, 114-117 (2013).
5. Kim, S. et al. Experimental demonstration of a second-order memristor and its ability to biorealistically implement synaptic plasticity. *Nano Lett.* **15**, 2203-2211 (2015).
6. Chen, H., Cai, Y., Han, Y. & Huang, H. Towards Artificial Visual Sensory System: Organic Optoelectronic Synaptic Materials and Devices. *Angew. Chem. Int. Ed. Engl.*, e202313634 (2023).
7. Gong, Y. et al. Bioinspired Artificial Visual System Based on 2D WSe<sub>2</sub> Synapse Array. *Adv. Funct. Mat.* **33**, 2303539 (2023).
8. Chen, S., Lou, Z., Chen, D. & Shen, G. An Artificial Flexible Visual Memory System Based on an UV-Motivated Memristor. *Adv. Mater.* **30**, 1705400 (2018).
9. Seo, S. et al. Artificial optic-neural synapse for colored and color-mixed pattern recognition. *Nat. Commun.* **9**, 5106 (2018).
10. Wang, W. et al. Artificial Optoelectronic Synapses Based on TiN<sub>x</sub>O<sub>2-x</sub>/MoS<sub>2</sub> Heterojunction for Neuromorphic Computing and Visual System. *Adv. Funct. Mat.* **31**, 2101201 (2021).
11. Yang, C. M. et al. Bidirectional All-Optical Synapses Based on a 2D Bi<sub>2</sub>O<sub>2</sub>Se/Graphene Hybrid Structure for Multifunctional Optoelectronics. *Adv. Funct. Mat.* **30**, 2001598 (2020).
12. Zhou, F. et al. Optoelectronic resistive random access memory for neuromorphic vision sensors. *Nat. Nanotechnol.* **14**, 776-782 (2019).
13. Tan, H. et al. An optoelectronic resistive switching memory with integrated demodulating and arithmetic functions. *Adv. Mater.* **27**, 2797-2803 (2015).

14. Xu, L. et al. N:ZnO/MoS<sub>2</sub>-heterostructured flexible synaptic devices enabling optoelectronic co-modulation for robust artificial visual systems. *Nano Res.* 1-11 (2023).
15. Liang, K. et al. Fully Printed Optoelectronic Synaptic Transistors Based on Quantum Dot-Metal Oxide Semiconductor Heterojunctions. *ACS Nano* **16**, 8651-8661 (2022).
16. Lee, G. et al. Artificial Neuron and Synapse Devices Based on 2D Materials. *Small* **17**, e2100640 (2021).
17. Pitaro, M., Tekelenburg, E. K., Shao, S. & Loi, M. A. Tin Halide Perovskites: From Fundamental Properties to Solar Cells. *Adv. Mater.* **34**, e2105844 (2022).
18. Wang, H. & Kim, D. H. Perovskite-based photodetectors: materials and devices. *Chem. Soc. Rev.* **46**, 5204-5236 (2017).
19. Zhu, X., Lee, J. & Lu, W. D. Iodine Vacancy Redistribution in Organic-Inorganic Halide Perovskite Films and Resistive Switching Effects. *Adv. Mater.* **29**, 1700527 (2017).
20. Xiao, Z. & Huang, J. Energy-Efficient Hybrid Perovskite Memristors and Synaptic Devices. *Adv. Electron. Mater.* **2**, 1600100 (2016).
21. Xiao, X. et al. Recent Advances in Halide Perovskite Memristors: Materials, Structures, Mechanisms, and Applications. *Adv. Mater. Technol.* **5**, 1900914 (2020).
22. Gu, C. & Lee, J. S. Flexible Hybrid Organic-Inorganic Perovskite Memory. *ACS Nano* **10**, 5413-5418 (2016).
23. Hong, X., Liu, X., Liao, L. & Zou X. Review on metal halide perovskite-based optoelectronic synapses. *Photon. Res.* **11**, 787-807 (2023).
24. Ham, S. et al. Photonic Organolead Halide Perovskite Artificial Synapse Capable of Accelerated Learning at Low Power Inspired by Dopamine-Facilitated Synaptic Activity. *Adv. Funct. Mater.* **29**, 1806646 (2018).
25. Yin, L. et al. Optically Stimulated Synaptic Devices Based on the Hybrid Structure of Silicon Nanomembrane and Perovskite. *Nano Lett.* **20**, 3378-3387 (2020).
26. Hao, D. et al. Lead-Free Perovskites-Based Photonic Synaptic Devices with Logic Functions. *Adv. Mater. Technol.* **6**, 2100678 (2021).
27. Huang, W. et al. Zero-power optoelectronic synaptic devices. *Nano Energy* **73**, 104790 (2020).
28. Zhao, P. et al. Self-powered optoelectronic artificial synapses based on a lead-free perovskite film for artificial visual perception systems. *J. Mater. Chem. C* **11**, 6212-6219 (2023).
29. Kandel, E. R. & Squire, L. R. Neuroscience: Breaking Down Scientific Barriers to the Study of Brain and Mind. *Science* **290**, 1113-1120 (2000).
30. Bi, G.-q & Poo, M.-m Synaptic modifications in cultured hippocampal neurons: dependence on spike timing, synaptic strength, and postsynaptic cell type. *J. Neurosci.* **18**, 10464-10472 (1998).
31. Favuzzi, E. et al. GABA-receptive microglia selectively sculpt developing inhibitory circuits. *Cell* **184**, 4048-4063 (2021).
32. Wu, Y. K., Miehl, C. & Gjorgjieva, J. Regulation of circuit organization and function through inhibitory synaptic plasticity. *Trends Neurosci.* **45**, 884-898 (2022).
33. Qian, C. et al. Solar-stimulated optoelectronic synapse based on organic

- heterojunction with linearly potentiated synaptic weight for neuromorphic computing. *Nano Energy* **66**, 104095 (2019).
34. Park, H. L. et al. Retina-Inspired Carbon Nitride-Based Photonic Synapses for Selective Detection of UV Light. *Adv. Mater.* **32**, 2005582 (2020).
  35. Hu, L. et al. All-Optically Controlled Memristor for Optoelectronic Neuromorphic Computing. *Adv. Funct. Mater.* **31**, 2005582 (2021).
  36. Liang, J. et al. All-Optically Controlled Artificial Synapses Based on Light-Induced Adsorption and Desorption for Neuromorphic Vision. *ACS Appl. Mater. Interfaces* **15**, 9584-9592 (2023).
  37. Zhang, M. et al. Improving the performance of ultra-flexible perovskite photodetectors through cation engineering. *J Phys D: Appl Phys* **53**, 235107 (2020).
  38. Wang, S. et al. Credible evidence for the passivation effect of remnant  $\text{PbI}_2$  in  $\text{CH}_3\text{NHCH}_3\text{PbICH}_3$  films in improving the performance of perovskite solar cells. *Nanoscale* **8**, 6600–6608 (2016).
  39. Wang, C. et al. Compositional and morphological engineering of mixed cation perovskite films for highly efficient planar and flexible solar cells with reduced hysteresis. *Nano Energy* **35**, 223–232 (2017).
  40. Lin, X. et al. In situ growth of graphene on both sides of a Cu–Ni alloy electrode for perovskite solar cells with improved stability. *Nat. Energy* **7**, 520–527 (2022).
  41. Kato, Y. et al. Silver Iodide Formation in Methyl Ammonium Lead Iodide Perovskite Solar Cells with Silver Top Electrodes. *Adv. Mater. Interfaces* **2**, 1500195 (2015).
  42. Xiong, J. et al. Interface Degradation of Perovskite Solar Cells and its Modification using an Annealing-free  $\text{TiO}_2$  NPs Layer. *Organic Electronics* **30**, 30-35 (2016).
  43. Lin, X. et al. Efficiency progress of inverted perovskite solar cells *Energy Environ Sci* **13**, 3823-3847 (2020).
  44. Govindacharyulu, P. A. & Bose, D. N. Photoconductivity in p-AgI. *Phys. Rev. B* **19**, 6532-6541 (1979).
  45. Sabeth, F., Iimori, T. & Ohta N. Gigantic Photoresponse and Reversible Photoswitching in Ionic Conductivity of Polycrystalline  $\beta\text{-AgI}$ . *J. Phys. Chem. C* **116**, 9209–9213 (2012).
  46. Naik, S. G. & Rabinal, M. H. K. Significance of electrode contact area on memristive parameters of silver iodide. *Mater. Sci. Semicond. Process.* **138**, 106309 (2022).
  47. Cho, D.-Y., Tappertzhofen, S., Waser, R. & Valov, I. Chemically-inactive interfaces in thin film Ag/AgI systems for resistive switching memories. *Sci Rep* **3**, 1169 (2013).
  48. Naik, S. G. & Rabinal, M. H. K. Compositional tuning of negative differential resistance in a bulk silver iodide memristor. *New J. Chem.* **45**, 1667-1676 (2021).
  49. Cai, K., Sun, J., Li, B. & J. Zhou. Hysteretic Current-Voltage Characteristics and Memristive Behaviors in AgI Nano-Particles Assembly. *ECS J. Solid State Sci. Technol.* **2**, N6-N10 (2013).
  50. Kong, S. & Shore, J. D. Modeling the Impact of Silver Particle Size and Morphology on the Covering Power and Tone of Photothermographic Media. *J. Imaging Sci. Technol.* **51**, 197-242 (2007).
  51. Quintero, B. D. et al. The Degradation of Daguerreotypes and the Relationship with Their Multi-Material Structure: A Multimodal Investigation. *Sensors* **23**, 4341 (2023).

52. Xing, J. et al. Ultrafast ion migration in hybrid perovskite polycrystalline thin films under light and suppression in single crystals. *Phys. Chem. Chem. Phys.* **18**, 30484-30490 (2016).
53. Strukov, D. B., Snider G. S., Stewart D. R. & Williams R. S. The missing memristor found. *Nature* **453**, 80-83 (2008).
54. Kolb, H., Fernandez, E. & Nelson, R. *Webvision: The Organization of the Retina and Visual System* (University of Utah Health Sciences Center, Salt Lake City (UT), 1995).
55. Ge, S. et al. Silver Iodide Induced Resistive Switching in CsPbI<sub>3</sub> Perovskite-Based Memory Device. *Adv. Mater. Interfaces* **6**, 1802071 (2019).
56. Ouyang, X. et al. Mechanisms of blue light-induced eye hazard and protective measures: a review. *Biomedicine & Pharmacotherapy* **130**, 110577 (2020).
57. Shinhmar, H., Hogg, C., Neveu, M. & Jeffery, G. Weeklong improved colour contrasts sensitivity after single 670 nm exposures associated with enhanced mitochondrial function. *Sci Rep* **11**, 22872 (2021).
58. Liu, G. et al. Organic Biomimicking Memristor for Information Storage and Processing Applications. *Adv. Electron. Mater.* **2**, 1500298 (2016).
59. Martin, L. C. *Nature* **99**, 365-366 (1917).
60. Guo, H. et al. Impact of halide stoichiometry on structure-tuned formation of CH<sub>3</sub>NH<sub>3</sub>PbX<sub>3-a</sub>Y<sub>a</sub> hybrid perovskites. *Solar Energy* **158**, 367–379 (2017).

## Acknowledgements

---

The authors acknowledge financial support from the National Natural Science Foundation of China (No. 61975148, No. 62375200). The authors acknowledge Assoc. Prof. Xinjun Liu for his guidance on the testing methods of memristors. The authors acknowledge Assoc. Prof. Zhixiang Sun and Assoc. Prof. Fan Yang for help with Glovebox System.

## Supplementary Information

---

Supplementary Information accompanies this paper at

## Supplementary Files

This is a list of supplementary files associated with this preprint. Click to download.

- [Supplementaryinformation.docx](#)